THE JOURNAL OF PHYSICAL CHEMISTRY C

Article

pubs.acs.org/JPCC

Surface Plasmon Resonance Imaging Microscopy of Liposomes and Liposome-Encapsulated Gold Nanoparticles

Lauri Viitala,[†] Adam M. Maley,[‡] H. W. Millie Fung,[‡] Robert M. Corn,[‡] Tapani Viitala,[§] and Lasse Murtomäki*[,†]

[†]Department of Chemistry, Aalto University. P.O. Box 16100, FI-00076 Aalto, Finland

[‡]Department of Chemistry, University of California—Irvine, Irvine, California 92697, United States

[§]Faculty of Pharmacy, University of Helsinki, P.O. Box 56, FI-00014 Helsinki, Finland

Supporting Information

ABSTRACT: Liposomes are small vesicles that can be used in various targeting applications as carrier vehicles. In this paper, we show that real-time surface plasmon resonance imaging microscopy (SPRI microscopy) can be used to detect diffraction patterns of these singular vesicles in water phase at room temperature and without any additives. The diffraction pattern intensities, related to the particle size, are shown to follow the log-normal distribution in a cumulative distribution function (CDF) that is very well in accordance with the normal size distribution of liposomes prepared with the extrusion method. In addition, this distribution is further analyzed to determine the number of gold nanoparticle (GNP) encapsulated liposomes in a set of liposomal adsorption events. Thus, we obtain the encapsulation efficiency and present a method to study the intrinsic properties of liposomes and other soft nanomaterials.

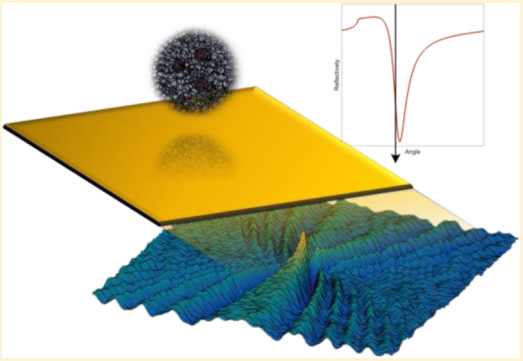

INTRODUCTION

Surface plasmon resonance (SPR) is a standard technique for the study of surface phenomena occurring on a plasmonic metal (i.e., Au, Ag, or Cu). These surface phenomena are manifested via the change in the average refractive index of a surface film. As the refractive index changes, the SPR angle (i.e., the angle in which the reflected beam has its lowest intensity) is also shifted, and the change can be detected according to the measurement setup. If the angle of the incident is fixed to a value between the critical and the SPR angle, i.e., to the configuration that is usually referred as SPR imaging (SPRI), the refractive index change is detected as an intensity change in the reflected beam. This information can be used to characterize the formation of various surface films and to study the specific interactions between macromolecules (e.g., DNA, RNA, and proteins).[1] In SPRI microscopy, the measurement setup is similar to the SPRI, but the surface plasmon polaritons (SPPs) are excited locally[2,3] and the reflection is collected as a microscope image. This can be achieved by using an objective with a high numerical aperture (NA) that possess multiple advantages in comparison to the normal SPR prism-coupled SPR microscopy that may suffer from distortion at the long working distances (see, e.g., refs 4−6). The high NA objective outputs collimated light that is set to an incident angle when the light beam is focused to the offset of the objective's back focal plane (BFP).[7] This angle can be further adjusted with a knife-edge mirror located before the BFP. When light is reflected from the sample, it enters the same high NA objective and passes to the detector where the image is constructed. In this way, Brownian motion of micron-sized particles,[8] viruses,[9] gold nanoparticle bound via ss-DNA hybridization[10] and peptide and protein uptake into singular hydrogel nanoparticles[11,12] has been studied previously, for example. The concentration regime for the nanosized particles is typically between 50 fM[10] and 60 pM,[11] since the nanoscale imaging resolution is only possible in very dilute systems.

Liposomes are soft nanomaterials that are constructed from lipids that are amphiphilic and form bilayered spherical structures by self-assembly in an aqueous phase. Liposome itself holds a cavity of another aqueous phase within the bilayer which can be utilized to drug delivery by encapsulating drug molecules, for instance. Liposomes can be made responsive to various endogenous (i.e., pH, enzymatic concentrations, etc.) and exogenous stimuli (i.e., temperature, electro-magnetic fields, etc.) using stimuli-sensitive lipids in the bilayer.[13,14] One of the most interesting external triggers is light. In this case, sensitivity to light can be obtained by encapsulating gold nanoparticles (GNPs) into the cavity of the liposomes where they act as photothermal agents during the illumination.[15] As liposomes are generally small and function only in the water phase, their study *in situ* may be difficult. In this paper, we introduce the SPRI microscope as one potential technique in

Received: September 20, 2016
Revised: October 27, 2016
Published: October 31, 2016

DOI: 10.1021/acs.jpcc.6b09503
J. Phys. Chem. C 2016, 120, 25958−25966

the study of soft nanomaterials such as liposomes. This can be done label-free, in real time and at room temperature by detecting single liposomes on 11-Mercaptoundecylamine (MUAM) and streptavidin functionalized surfaces. The single liposome diffraction patterns are located and analyzed with a new phenomenological theory introducing the field enhancement effect emerging form the surface binding of the particles. These results are then used to build up an empirical cumulative distribution function (ECDF), from where the number of liposomes containing encapsulated GNPs is determined.

THEORY

Reflection Image Formation in the SPRI Microscope. The electrodynamics of time harmonic linear media are described by Maxwell's equations:

$$\begin{aligned} &\text{(i)}\quad \nabla \times \vec{E} = -i\omega\mu\vec{H} \\ &\text{(ii)}\quad \nabla \times \vec{H} = \vec{J}_f + i\omega\epsilon\vec{E} \end{aligned} \tag{1}$$

Applying the curl operator ($\nabla\times$) leads to the Lagrange's equation:

$$\nabla \times \nabla \times \vec{E} = \nabla(\nabla\cdot\vec{E}) + \nabla^2\vec{E} = -i\omega\mu\vec{J}_f - \omega^2\mu\epsilon\vec{E} \tag{2}$$

where the free current density ($\vec{J}_f$) determines how good a conductor the material is. In the case of metals, it is determined by the Ohm's law

$$\vec{J}_f = \sigma\vec{E} \tag{3}$$

and the free charge density becomes negligible (i.e., $\nabla\cdot\vec{E} = 0$). Thus, eq 2 can be expressed as

$$(\nabla^2 + \omega^2\mu\epsilon + i\omega\mu\sigma)\vec{E} = (\nabla^2 + \tilde{k}^2)\vec{E} = 0 \tag{4}$$

where $\tilde{k}^2 = \omega^2\mu\epsilon + i\omega\mu\sigma = (k + \kappa i)^2$ is the square of the complex wavenumber. When particles are adsorbed to the surface, the electric current density is altered, and these particles can be seen as a set of individual dipoles. The electric current density formed by these dipoles is of the form:[16]

$$\vec{J}_F = -i\omega\sum_{n=1}^{N}\vec{p}_n\,\delta(\vec{r}_n) \tag{5}$$

where $\vec{r}_n = \vec{r} - \vec{r}_n$ and $\vec{r}_n$ is the adsorption site of the nth dipole and δ is the delta function. Here we have assumed that the effect is nonmagnetic ($\nabla \times \vec{M} = 0$) and the function emerges from the first time derivative of the electric polarizations. When a single particle is detected in a microscope, we may approximate that the displacement current density is of the form:

$$\vec{J}_p = \frac{\partial}{\partial t}\vec{p}_p\,\delta(\vec{r}) = -iq\vec{E}_{ext}\delta(\vec{r}) \tag{6}$$

where $\vec{p}_p$ is the effective dipole moment of a single particle at the adsorption site and q is the effective magnitude of the polarization current (assumed isotropic) driven by the exciting electric field $\vec{E}_{ext}$ that can be assumed to be uniform. By adding eq 6 to eq 2, we get

$$(\nabla^2 + \tilde{k}_c^{\,2})\vec{E} = -Q\vec{E}_{ext}\delta(\vec{r}) \tag{7}$$

where Q is the source term and $\tilde{k}_c$ is the detectable complex wavenumber of the composite. The solution can be obtained by a Green function (G) that satisfies

$$(\nabla^2 + \tilde{k}_c^{\,2})G = -\delta(\vec{r}) \tag{8}$$

Formally, the solution for the electric field is achieved by a dyad $\vec{\vec{g}} = \left(1 + \frac{1}{\tilde{k}_c^{\,2}}\nabla\nabla\cdot\right)G\vec{\vec{I}}$.[17] In the current case here, however, we only focus on the planar wave propagation in cylindrical symmetry without θ-dependency and occurring only at the surface (i.e., $z = 0$). Hence, the problem can be reduced to the r component alone, and the scalar solution ϕ is essentially the reflection from the surface:

$$\phi = \frac{|\vec{E}|}{|\vec{E}_{ext}|} = |Q\int_{V'} G(\vec{r}\,')\delta(\vec{r} - \vec{r}\,')\,dV'| = |QG(\vec{r})| \tag{9}$$

It is clear that the corresponding reflection is a constituent of multiple contributions. For instance, these contributions are surface and particle interactions; SPP propagation; light polarization; etc.[17−19] In order to simplify matters, we may use the following approximation (following ref 16):

$$\phi = |\phi_1 + \phi_2| = |Q_1'G_1 + Q_2'G_2| \tag{10}$$

where ϕ_1 is the solutions for the primary field (i.e., 1D solution describing the SPP propagation on a clean surface):

$$\phi_1 = -iQ_1'\sqrt{\frac{\pi}{2}}\frac{1}{\tilde{k}_c}e^{-i\tilde{k}_c x},\ x = |x - x_0| \tag{11}$$

and ϕ_2 is the secondary field term describing the scattering effect (i.e., the particle interaction). Q_1' and Q_2' are the source factors and G_1 and G_2 are the corresponding Green functions. The solution for the scattering part is achieved from the $\mathbb{R}^2$ inverse Fourier transform:

$$\phi_2(\vec{r}) = \frac{Q_2'}{4\pi^2}\int_{\mathbb{R}^2} e^{-i\vec{\omega}\cdot\vec{r}}(\omega^2 - \tilde{k}_c^{\,2})^{-1}\,d\omega^2 \tag{12}$$

that can be solved by using the following definitions of the well-known Bessel functions ((i) p 921, eq 7; (ii) p 679, eq 4; and (iii) p 920, eq 2 in ref 20):

$$\begin{aligned} &\text{(i)}\quad J_0(z) = \frac{1}{\pi}\int_0^{\pi} e^{\pm iz\cos\tau}\,d\tau \\ &\text{(ii)}\quad K_0(ak) = \int_0^{\infty} J_0(a\tau)\tau(\tau^2 + k^2)^{-1}\,d\tau \\ &\text{(iii)}\quad K_0(z) = -\frac{\pi i}{2}H_0^{(2)}(-iz) \end{aligned} \tag{13}$$

This solution is

$$\begin{aligned} \phi_2(\vec{r}) &= \frac{Q_2'}{4\pi^2}\int_0^{\infty}\left[\int_0^{2\pi}\frac{e^{-i\omega r\cos\theta}}{\omega^2 - \tilde{k}_c^{\,2}}\,d\theta\right]\vec{\omega}\,d\vec{\omega} \\ &= \frac{Q_2'}{2\pi}\int_0^{\infty}\frac{J_0(\omega_r r)\omega_r\,d\omega_r}{\omega_r^2 + \tilde{k}'^2} = \frac{Q_2'}{2\pi}K_0(\tilde{k}'r) \Leftrightarrow \phi_2(\vec{r}) \\ &= -\frac{iQ_2'}{4}H_0^{(2)}(\tilde{k}_c r) \end{aligned} \tag{14}$$

where we have used a variable change $\tilde{k}' = i\tilde{k}_c$ in the second integrand and $H_0^{(2)}$ is the zeroth order Hankel function of second kind. The full solution in Cartesian coordinates is then

$$\phi(x, y) = |iQ_1\tilde{k}_c^{-1}e^{-i\tilde{k}_c x} + iQ_2H_0^{(2)}(\tilde{k}_c\sqrt{x^2 + y^2})| \tag{15}$$

where Q_1 and Q_2 are the field enhancement factors.

DOI: 10.1021/acs.jpcc.6b09503
J. Phys. Chem. C 2016, 120, 25958−25966

Difference Image Analyses. The difference images in the SPRI microscope are constructed pixel-by-pixel according to equation

$$I^{\{x,y\}}(t_2) = \frac{I'^{\{x,y\}}_{t_2} - I'^{\{x,y\}}_{t_1}}{I'^{\{x,y\}}_{t_1}} \tag{16}$$

where $I'^{\{x,y\}}_{t_i}$ is the intensity of a single pixel at the time point t_i; located at $\{x, y\}$ in the raw image. The next image is taken in three second intervals, so that $t_{i+1} - t_i = 3$ s. We can derive the difference image intensity equation based on the concepts of the primary and the secondary fields ($\vec{E}_1$ and $\vec{E}_2$), since the intensity is directly proportional to $\vec{E}\cdot\vec{E}^*$ (the superscript * is the notation for the complex conjugate).[21] When a particle is partly present in both raw images with timely proportions β_1 and β_2, respectively, the raw image intensities have a relation with the fields

$$I'_{t_1} \propto (\vec{E}_1 + \beta_1\vec{E}_2)\cdot(\vec{E}_1 + \beta_1\vec{E}_2)^* = |\vec{E}_1|^2 + \beta_1^2|\vec{E}_2|^2 + 2\beta_1\mathcal{R}e(\vec{E}_1^*\cdot\vec{E}_2) \text{ and}$$

$$I'_{t_2} \propto (\vec{E}_1 + \beta_2\vec{E}_2)\cdot(\vec{E}_1 + \beta_2\vec{E}_2)^* = |\vec{E}_1|^2 + \beta_2^2|\vec{E}_2|^2 + 2\beta_2\mathcal{R}e(\vec{E}_1^*\cdot\vec{E}_2) \tag{17}$$

$$\text{where } 2\mathcal{R}e(\vec{E}_1^*\cdot\vec{E}_2) = 2[\mathcal{R}e(\vec{E}_1)\mathcal{R}e(\vec{E}_2) + \mathcal{I}m(\vec{E}_1)\mathcal{I}m(\vec{E}_2)] = 2\mathcal{R}e(E_1^*E_2\cos\theta)$$

(where θ is the angle between two propagations). The difference image can therefore be expressed as

$$I \propto \frac{(\beta_2^2 - \beta_1^2)|\vec{E}_2|^2 + 2(\beta_2 - \beta_1)\mathcal{R}e\{E_1^*E_2\cos\theta\}}{|\vec{E}_1|^2 + \beta_1^2|\vec{E}_2|^2 + 2\beta_1\mathcal{R}e\{E_1^*E_2\cos\theta\}} \tag{18}$$

Since the field $\vec{E}_1$ is strong when compared with $\vec{E}_2$, the difference image is highly angular-dependent: like reported earlier by Watanabe et al. in the case of localized plasmon propagation.[22] To simplify matters, we may also assume that the secondary field contribution emerge only in the latter image ($\beta_1 = 0$, $\beta_2 = 1$):

$$I'_{t_1} \propto \vec{E}_1\cdot\vec{E}_1^* = |E_1|^2 \text{and}$$

$$I'_{t_2} \propto (\vec{E}_1 + \vec{E}_2)\cdot(\vec{E}_1 + \vec{E}_2)^* \tag{19}$$

giving the difference image

$$I \propto \frac{|E_2|^2 + 2\mathcal{R}e\{\vec{E}_1^*\cdot\vec{E}_2\}}{|E_1|^2} = \frac{|\vec{E}_2|^2 + 2\mathcal{R}e\{E_1^*E_2\cos\theta\}}{|\vec{E}_1|^2} \tag{20}$$

It should be noted that eqs 20 and 18 can be interpreted slightly differently from one another. Whereas eq 18 can be used to determine the absolute value of the adsorption events with time as a variable, eq 20 determines the relative intensity change in a fixed time span. Both of these equations can be used in the data analyses of SPRI microscope images. However, since more than one indistinguishable adsorption event can occur in the three second time interval, and these events will blend to a statistical distribution by default, it is more preferable to use eq 20 rather than eq 18 that carries a risk factor of overparametrization. Hence, this choice can be justified with the law of parsimony (i.e., Occam's razor, see, e.g., ref 23).

MATERIALS AND METHODS

Materials. 1,2-Dipalmitoyl-*sn*-glycero-3-phosphocholine (DPPC) was purchased from Sigma-Aldrich; 1,2-distearoyl-*sn*-glycero-3-phosphoethanolamine-*N*-[amino(polyethylene glycol)-2000] (DSPE-PEG) and 1,2-dipalmitoyl-*sn*-glycero-3-phosphoethanolamine-*N*-(biotinyl) (DPPE-Biotin) from Avanti Polar Lipids, Inc.; and *N*-(fluorescein-5-thiocarbamoyl)-1,2-dihexadecanoyl-*sn*-glycero-3-phosphoethanolamine (DHPE-Fluorescein) from Thermofisher Scientific. Unconjugated gold nanoparticles (GNPs) of diameters 10 and 40 nm were purchased from Ted Pella, Inc.. 11-Amino-1-undecanethiol hydrochloride (MUAM) was purchased from Dojindo Molecular Technologies, Inc.. EZ-Link NHS-PEG$_4$-biotin and 1-ethyl-3-(−3-(dimethylamino)propyl) carbodiimide hydrochloride (EDC) were purchased from Thermofisher Scientific. Sephadex G-50 gel and other chemicals were purchased from Sigma-Aldrich unless otherwise stated.

Preparation and Characterization of Liposomes. Total concentration of ca. 1.5 μmol of the composition DPPC:DSPE-PEG:DPPE-Biotin:DHPE-Fluorescein 90:3:7:0.5 of lipids in chloroform were added to a round flask. The chloroform was evaporated under a stream of nitrogen. During the nitrogen flow, the temperature was slowly increased to ca. 60 °C, and the evaporation was continued for another 30 min in this temperature. Next, the film was hydrated under sonication with commercial phosphate buffered saline, PBS (11.9 mM phosphate buffer, 13.7 mM sodium chloride, 2.7 mM potassium chloride, pH 7.4, Fisher), containing the encapsulated material (i.e., GNPs) at 60 °C. The total volume of the added solution was 750 μL, hence resulting in a solution with a total lipid concentration of ca. 2.1 mM. Liposomes were then extruded 11 times ($T \approx 60$ °C) through double-stacked polycarbonate membranes (PC membranes, Avanti Polar Lipids, Inc.) with pore sizes of 400 nm and then 11 times through PC membranes with pore sizes of 200 nm. Extrusion reduces the lamellarity (i.e., the number of "nested" bilayers) in the liposomes and increases the total encapsulation volume. After the extrusion, lipids were stored at 4 °C and were used within 2 weeks after preparation. Before every measurement, these stock solutions were eluted through a gel filter column (Sephadex G-50) to remove any excess nanoparticles and other impurities. The primary aliquot, containing most of the liposomes, was detected by the naked eye under the UV light during the elution. The accurate concentration was determined by a spectrofluorometer (JASCO Analytical Instruments model JASCO FP-6300) by measuring the fluorescein (FC) emission intensity at wavelength 515 nm with excitation at 495 nm (see the Supporting Information). The sample was then diluted to approximately 20 pM for the SPRI microscope measurement.

Preparation of the Substrate. SF10 glass slides (Schott Glass) were used in all studies. First, plasma cleaned glass surfaces were silanized with Sigmacote using the manufacturer's protocol. Next, a Denton DV 502-A evaporator was used to deposit an adhesion layer of chromium (1 nm) onto the glass surface. This was followed by depositing a 45 nm layer of gold with the same technique. Hereafter, the slides were rinsed with ethanol and immersed into 1 mM ethanolic solution of MUAM. After 18 h, the MUAM coated slides were washed again and used as such. To prepare streptavidin functionalized surfaces, the MUAM coated glass slides were washed and treated with 2 mg mL^{-1} poly-L-glutamic acid sodium salt (50 000−100 000 g mol^{-1}) solution for 30−40 min. Then, 2-

DOI: 10.1021/acs.jpcc.6b09503
J. Phys. Chem. C 2016, 120, 25958−25966

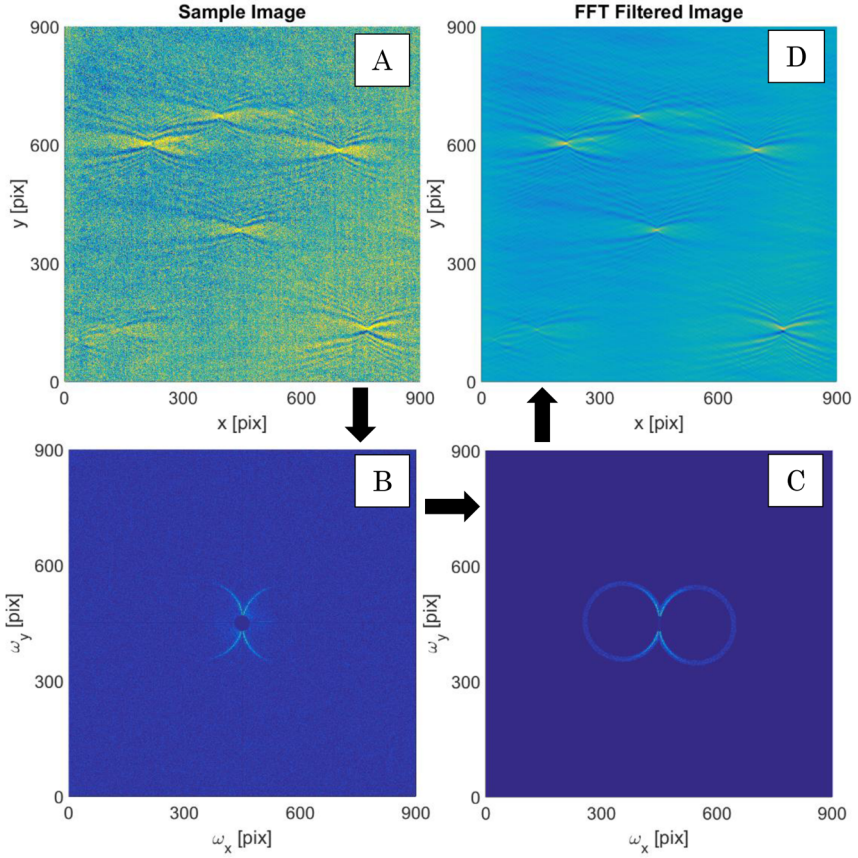

Figure 1. Image (liposomes on MUAM) processing in steps: (1) raw sample image (inset A) is formed after eq 21; image is Fourier transformed (inset B) and the noise is filtered from the FFT image (inset C). The resulting FFT filtered sample image (inset D) is achieved from the inverse Fourier transform. The circle in the middle of the FFT images is an additional mask that makes the circles more detectable. It has no function in the filtration process. The sample images in the SPRI microscope are in gray scale: false colors in the images are added in the after-treatment to help the visualization.

(*N*-morpholino)ethanesulfonic acid (MES, 55 mM) buffered solution (pH 5) of 4.5 mM of NHS-PEG$_4$-biotin and 25 mM of EDC was applied on the surface, and the solution was left there to react for approximately 3 h. The slides were then rinsed again with water before an adhesive microscope well grid made out of silicone (Electron Microscopy Sciences) was attached to the surface and the grid holes were filled with 10 μL of 100 μg mL^{-1} streptavidin in PBS. After 30 s, the slides were carefully rinsed with PBS, and the grid holes were filled again with PBS in order to focus the initial microscope image.

SPRI Microscopy of Liposomes. The optical setup in the SPRI microscope studies was similar to that described by Halpern et al.[10] earlier. Briefly, an IX51 inverted microscope (Olympus, Tokyo, Japan) was used as a frame of the microscope. A near-IR diode laser beam (1 mW, 814 nm, Melles Griot, Carlsbad, CA) was expanded and collimated using a spatial filter (Newport Corp., Newport Beach, CA) following a polarizer. The polarized light was then focused with a lens (f = 200 mm) and directed into the back focal plane of a 100 × 1.49 high numerical aperture objective (Olympus) with a gold-coated knife edge mirror (Thorlabs, Newton, NJ). The reflected image was then passed to an Andor Neo sCMOS camera (South Windsor, CT), where the image was constructed.

SPRI microscope raw images, each acquired by accumulating 30 11-bit images with 0.1 s exposure times, were subtracted pixel by pixel (at $\{x,y\}$) with one another with a self-made Matlab function (Supporting Information, "spri_m_fun.m"), resulting in three second difference images ($t_2 - t_1 = 3$ s)

$$I^{\{x,y\}}(t_2) = 100\frac{I'^{\{x,y\}}_{t_2} - I'^{\{x,y\}}_{t_1}}{I'^{\{x,y\}}_{t_1}} \tag{21}$$

that represent the relative change on the sensor surface in this time interval. As the difference images contain noise that can hide some of the particles, the image was noise-filtered with a fast Fourier transformation (FFT) based method. This was done in steps that are illustrated in Figure 1 and as follows. First, an FFT difference image is produced from a sample image (Figure 1A). The FFT image (Figure 1B) has a characteristic shape of a double sphere when particles are adsorbed to the surface. The unimportant noise is then filtered from the image by masking the inside and the outside areas of the FFT double spheres (Figure 1C). The size of these spheres depend on the complex wavenumber. This is obvious because $\tilde{k}_c^2 = \omega_x^2 + \omega_y^2$ determines the critical resonance condition in Fourier space. After the masking, an inverse FFT is produced, and the resulting image (Figure 1D) is used to detect the adsorbed particles manually with the same Matlab function. The maximum intensity points of each detected particle were listed and the intensity data surrounding the maximum intensity point was stored to a data matrix I_{particle} for the further data processing.

DOI: 10.1021/acs.jpcc.6b09503
J. Phys. Chem. C 2016, 120, 25958−25966

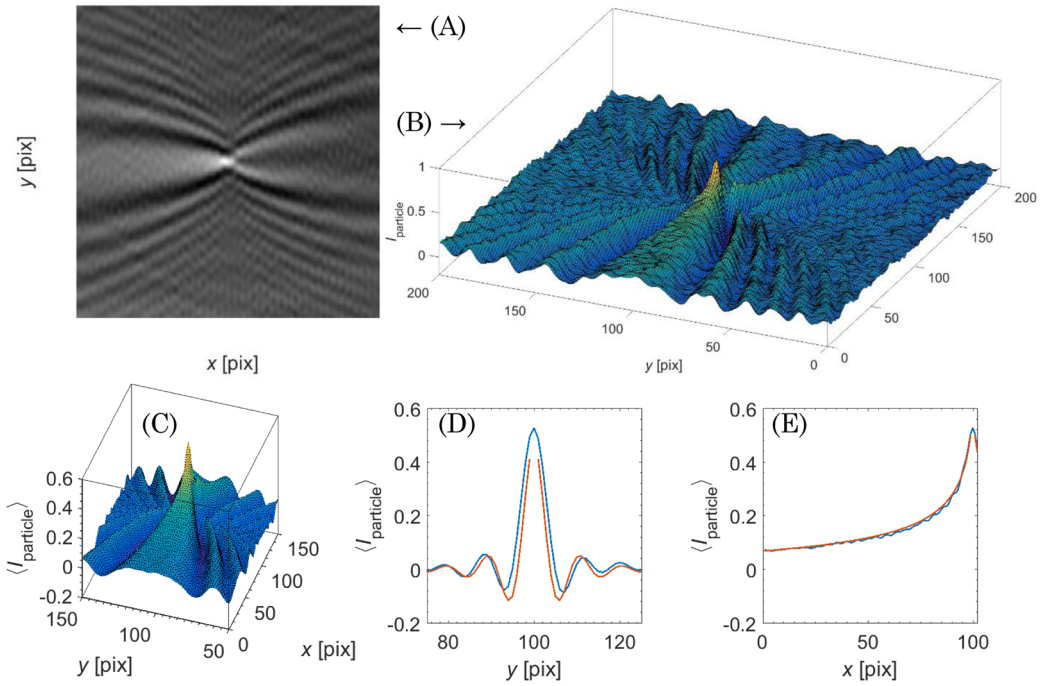

Figure 2. (A) Typical FFT filtered difference image of a liposome on the streptavidin surface. (B) Panel A as a surface plot. (C) The average of all liposome binding events. (D) The cross-section of C in the y direction (x at the maximum intensity, blue curve) with a fit with eq 24 (red curve). (E) The cross-section of C in the x direction (y at the maximum intensity, blue curve) with a fit with eq 25 (red curve).

In order to acquire more information on the adsorbing particles, the intensity data can be compared with a fitting function

$$I_{\text{particle}}^{\text{fit}} = I_{\text{b}} + \left[\upsilon^2 |\text{H}_0^{(2)}(\tilde{a}\sqrt{x^2+y^2})|^2 + 2\upsilon\mathcal{R}e\{-\text{iH}_0^{(2)}(\tilde{a}\sqrt{x^2+y^2})(-\text{i}\tilde{a}^{-1}\text{e}^{-\text{i}\tilde{a}x})^*\cos\theta\}\right] / [|1 - \text{i}\tilde{a}^{-1}\text{e}^{-\text{i}\tilde{a}x}|^2] \quad (22)$$

where $\upsilon = \frac{Q_2}{Q_1}$ is the intensity parameter (or field enhancement due to a particle), I_{b} is the intensity of the baseline and $\tilde{a} = a' + \text{i}a''$ is the complex wavenumber. Equation 22 is the equivalent form of eq 20. It is obtained by using the analogy of eqs 11 and 14 with the fields E_1 and E_2, respectively. In order to run fits from the singular adsorption patterns, the data matrices I_{particle} were cropped to form a 25 × 51 pixels wide image, where the maximum intensity point (x, y = 0) was located at the 26th pixel in the x axis and the 26th pixel in y axis. In other words, I_{particle} matrices only contain the primary propagation direction in the x axis. The fitting was done with a self-made Matlab script "spri_m_src.m" (Supporting Information) with 100 repetitions with random initial parameters and with 10 000 iterations with Levenberg−Marquardt algorithm. The goodness of the fit was estimated primarily with the sum of residues and secondarily with the Pearson correlation coefficient squared (R^2 = 1−det $\vec{R}$ (F, F_{fit}), where $\vec{R}$ is the result of "corrcoef" function in Matlab). Fittings with $R^2 \geq 0.64$ were further analyzed, whereas other results were disregarded. The maximum intensity point was left out from the fitting, as the theory applies only for the propagation away from the origin.

In addition to the fitting results, the intensity average of 9 pixels at the intensity maximum (minus the baseline intensity) were collected from the original FFT filtrated single particle image: $I_{\text{particle}}^{\text{max}} = \langle I_{\text{particle}}(x = -1, 0, 1, y = -1, 0, 1)\rangle - \langle\overline{I}\rangle$ (where $\langle\overline{I}\rangle$ is the median of the pixel intensities) and each data array was transformed to an empirical cumulative distribution function (ECDF) form. This was done by simply sorting the data from the smallest to largest value ($x = [x_1, x_2 \ldots x_n]$, where $x_1 \leq x_2 \ldots \leq x_n$) in the x-axis and by labeling these data points from n^{-1} to 1 ($y = [1, 2, \ldots, n]/n$, where n is the number of the detected particles) in the y-axis, respectively. Hereafter, the equation

$$P(x) = \frac{p_1}{2}\left(1 + \text{erf}\left(\frac{x - p_2}{\sqrt{2}p_3}\right)\right) \quad (23)$$

or the log-normal equivalent with replacement of x with ln x, was used to fit the ECDF assuming that a single particle-type exists in the system, but also with the assumption that two sets of particles are present. In the latter case, the ECDFs was fitted as a sum of two $P(x)$ functions.

As the standard distribution in nature is the normal distribution, the fact that the data is otherwise distributed is a characteristic feature of the system. The size distribution of liposomes that are prepared with the extrusion method, i.e., formed in a nonergodic condition, follow the (Gosset's) student-t distribution or log-normal distribution.[24] The log-normal distribution has benefits due to its simplicity, and it is used in this paper following the convention in most publications on liposomes today. As the size of the particles is directly proportional to the adsorption pattern intensity,[10] the intensity distribution of the liposomes should follow a log-normal distribution. This is why all intensity distributions were fitted with both the log-normal and normal CDFs (eq 23), as well as with one particle and two particles in the system. The results were compared, and the characteristic shape, number of particle-types, and the quantity of each particle types were determined.

DOI: 10.1021/acs.jpcc.6b09503
J. Phys. Chem. C 2016, 120, 25958−25966

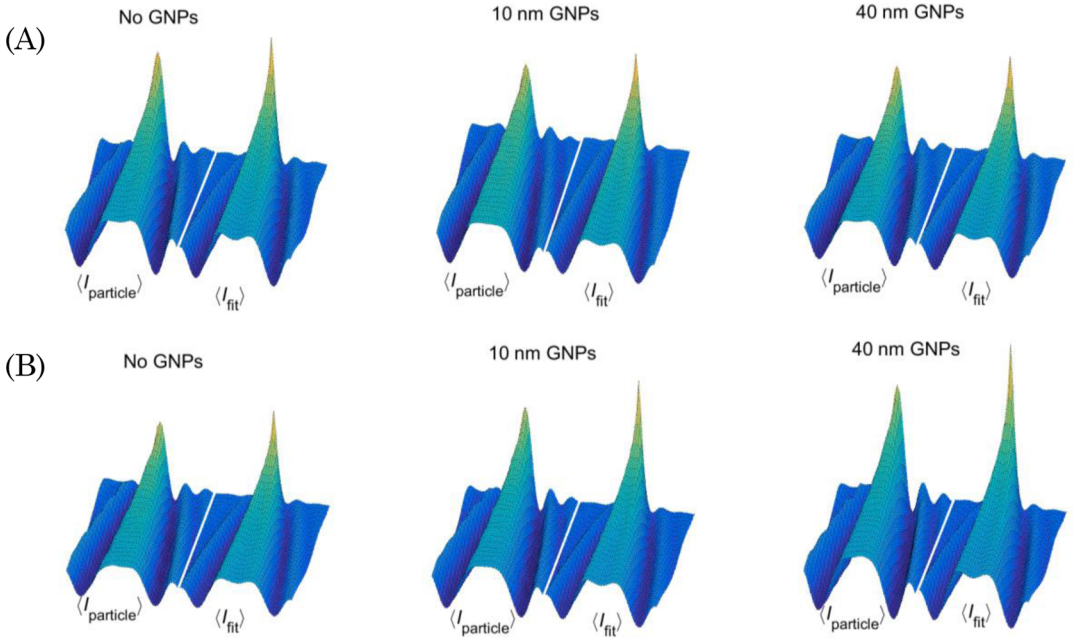

Figure 3. Average measured SPRI microscope intensity pattern $\langle I_{particle} \rangle$ next to the average fit $\langle I_{fit} \rangle$ of all liposomes without (left figures), with and without 10 nm GNPs (center), and with and without 40 nm GNPs (right) on (A) streptavidin coated surface and on (B) MUAM.

RESULTS AND DISCUSSION

Characteristics of the Diffraction Patterns of Single Liposomes. Typical SPRI microscope difference images of adsorbing liposome is presented in Figure 2A,B. In a typical case, the diffraction pattern appeared as a clear intensity maximum followed by a long and unified fanlike propagation pattern in the direction of the inherent plasmonic propagation. This pattern was surrounded by a multitude of contiguous surface waves on regular intervals. The back-propagation almost mirrors the forward pattern, but at the height of the intensity maximum of the particle, the pattern is duplexed into a two-edged form with the central line intensity being almost indistinguishable from the background. The average of all SPRI microscope difference images of the liposomes without encapsulated GNPs is shown in Figure 2C. Interestingly, when the average of the adsorbing patterns is sliced in x and y directions (Figure 2D,E) at the central line, the profile in the y-direction resembles a Bessel function, distinctly the zeroth order Bessel J. With relatively small υ values ($\upsilon^2 \approx 0$), the shape of the fitting function close to the adsorption site is of the form

$$f_y = \lim_{x \to 0} \mathcal{R}e\{-\mathrm{i}H_0^{(2)}(\tilde{a}\sqrt{x^2 + y^2})(-\mathrm{i}\tilde{a}^{-1}\mathrm{e}^{-\mathrm{i}\tilde{a}x})^*\} = \mathcal{R}e\{\tilde{a}^{-1}H_0^{(2)}(\tilde{a}|y|)\} \quad (24)$$

that is $\mathcal{R}e\{\tilde{a}^{-1}H_0^{(2)}(\tilde{a}|y|)\} \approx a'^{-1}J_0(a'|y|)$, when $\tilde{a} \approx a'$. However, when x is precisely zero, cos θ becomes zero and eq 22 becomes sharply peaked. This behavior differs from the observed one, but it can be understood as frailty of the theory near the origin (note! the theory only applies for the propagation away from the origin). In any case, our simplified approach can be fitted readily to the y-directional slice, as can be seen from Figure 2D. Similarly, the slice in the x direction (Figure 2E) shows characteristics of another Bessel function that resembles our fitting equation in the propagation side when

$$f_x = \lim_{y \to 0} \mathcal{R}e\{-\mathrm{i}H_0^{(2)}(\tilde{a}\sqrt{x^2 + y^2})(-\mathrm{i}\tilde{a}^{-1}e^{-\mathrm{i}\tilde{a}x})^*\mathrm{s}\} \quad (25)$$

As both, eqs 24 and 25, have a relation with $\mathcal{R}e\{\tilde{a}^{-1}\}$ near the origin, the maximum intensity close to the adsorption site $I_{particle}^{max}$ can be assumed to have a similar relation

$$I_{particle}^{max} \propto \mathcal{R}e\{\tilde{a}^{-1}\}\upsilon \quad (26)$$

Therefore, at least two direct contributions, particle size, that is most likely related to parameter υ, and the optical properties of the composite (i.e., $\tilde{a}$) play part in the maximum intensity values. Obviously, the fundamental reason to the intensity change in the SPRI is the change in the SPR angle. Hence, it is clear that parameter υ is also a function of a sort of the refractive index. As the derivation of this function is nontrivial, we leave it out from this paper and focus on the distributional analyses instead in the next chapters.

Detection of the Encapsulated GNPs inside Liposomes. Figure 3 shows the average difference images against the average of best fits for liposomes with and without encapsulated GNPs on a streptavidin coated surface (Figure 3A) and on a MUAM surface (Figure 3B). On a streptavidin surface, the intensity values were systematically lower when compared with the MUAM surface but the shape of the pattern was similar in both surfaces meaning that the average wave numbers had similar values. This is better depicted in Figure 4A,B that show the measured $I_{particle}^{max}$ values as an ECDF (black dots) and the corresponding $P(I_{particle}^{max})$ fit assuming that one (dashed lines) or two (continuous line) particle types are present. Similarly, Figure 4C,D represents the intensity parameter υ from the diffraction pattern fitting. On both surfaces and with both variables ($I_{particle}^{max}$ and υ), the ECDF of liposomes without GNPs (blue lines) can be fitted readily with just one particle-type. Liposomes with encapsulated GNPs, instead, have clear divergence from the one-particle-type fit at the relatively higher intensities. This enhancement is more prominent on MUAM surface where the liposomes reach closer

DOI: 10.1021/acs.jpcc.6b09503
J. Phys. Chem. C 2016, 120, 25958−25966

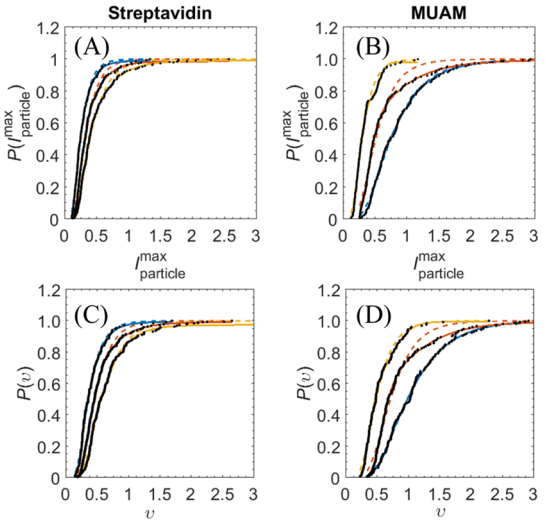

Figure 4. ECDF (black dots) of the measured SPRI microscope intensities $I^{max}_{particle}$ (A and B) and fitted parameters υ (C and D) for each detected liposome on streptavidin (left box) and on MUAM (right box) showing the best CDF fit $P(x)$ without GNPs (blue lines), with 10 nm GNPs (red lines), and with 40 nm GNPs (yellow lines) assuming one-particle-type (dashed lines) or two-particle-types (solid lines) are present in the liposome sample. The GNP-free samples were readily explicable with one-particle-type, whereas the liposomes with GNPs needed another particle-type to explain the shape of their ECDFs.

proximity to the SPP propagation. As the typical encapsulation efficiency of GNPs should be around 10−30% in liposomes prepared with the extrusion method, the diverging point in these figures are in line with the assumed encapsulation efficiency. In both GNP-containing samples, this value is close to 20%. More precisely, the fits diverge at 23% and 24% with 10 nm GNPs and 40 nm GNPs, respectively.

In addition to the intensity results, wavenumbers were readily obtained from the fitting. The real part of the wavenumber determines the number of contiguous waves originating from the adsorption center. The imaginary part shows how quickly the SPRI microscope pattern is dissipated to its surroundings. Since, the fitting of this parameter is done mostly outside of the region of the liposome adsorption (as the diameter of liposomes is only one-to-three pixels), it relates with the plasmonic propagation medium on which the microscope is initially focused. Hence, it is comprehensible that smaller and lower intensity particles do not show substantial wavenumber shifts or shift in a parameter $n_c = \mathcal{R}e\left\{\left(\frac{\lambda}{2\pi\zeta}\tilde{a}\right)^{-1}\right\}$ based on relation 26, where ζ = 92 nm/pix and λ = 814 nm. As this parameter centers close to unity with the liposomes (Figure 5A,B) and some other materials (unpublished results), it can be considered as a focus parameter. It is clear from Figures 3 and 4 that MUAM surfaces were more sensitive toward the detection of the intensity changes than the streptavidin coated surfaces. Hence, it is no surprise that the shifts in the index n_c were also easier to obtain on MUAM. This can be seen in Figure 5A that shows an asymmetrical shape for the ECDF curves with the liposome samples containing 10 and 40 nm GNPs on MUAM. Without GNPs (blue lines), the curve remained symmetrical and no diverging behavior was detected. On streptavidin, these curves were rather symmetrical with only a slight shift in the n_c parameter with the GNP-liposomes (Figure 5B). It is notable that the diverging point in the fits with one and two particle types for GNP-liposomes diverge close to the same value (close to 0.8) as the CDF of $I^{max}_{particle}$ in Figure 4.

Relation between Intensity Parameters and the Size Distribution. In the paper by Halpern et al.,[10] it was shown that the average $\Delta\%R$ ($I^{max}_{particle}$) was proportional with the average particle size, giving a log−log plot with a slope of approximately three against the particle size. Since the size distribution of liposomes, prepared with the extrusion method, is typically log-normally distributed and it contains a wide size range; the analyses of the averaged numbers can be quite inconclusive. Therefore, the best method is to compare the parameter in hand with the actual size distribution. Obviously, the determination of the exact size distribution can be difficult, but to illustrate the idea, we can use the size distribution determined with dynamic light scattering (DLS). Figure 6A shows the ECDF with the best one-particle-type fit $P(x)$ (solid lines) and the corresponding probability distribution function

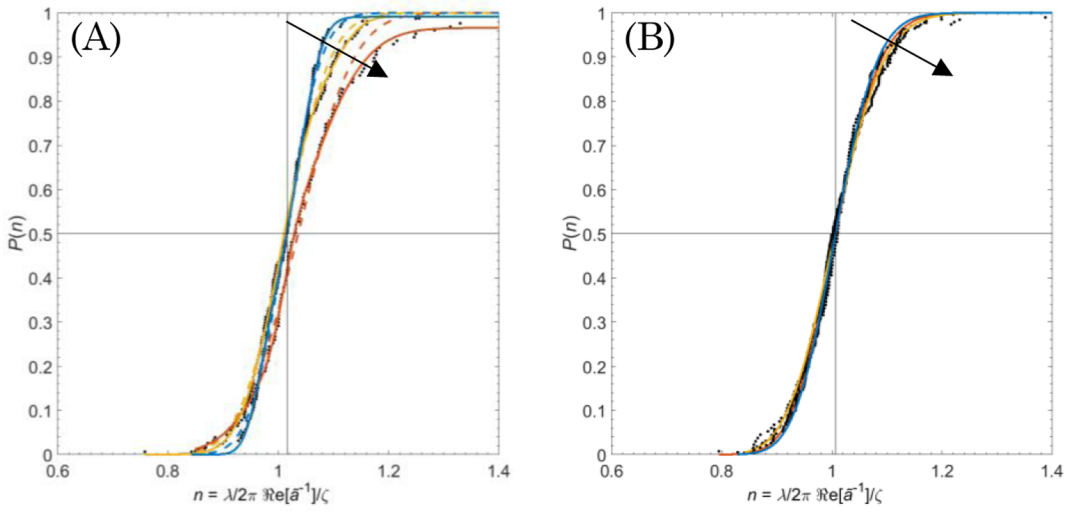

Figure 5. Empirical cumulative distribution function (ECDF) for parameter n_c on (A) MUAM and on (B) streptavidin coated surface. The arrows point out, how the distribution shifts to an asymmetrical form in GNP encapsulated liposomes.

DOI: 10.1021/acs.jpcc.6b09503
J. Phys. Chem. C 2016, 120, 25958−25966

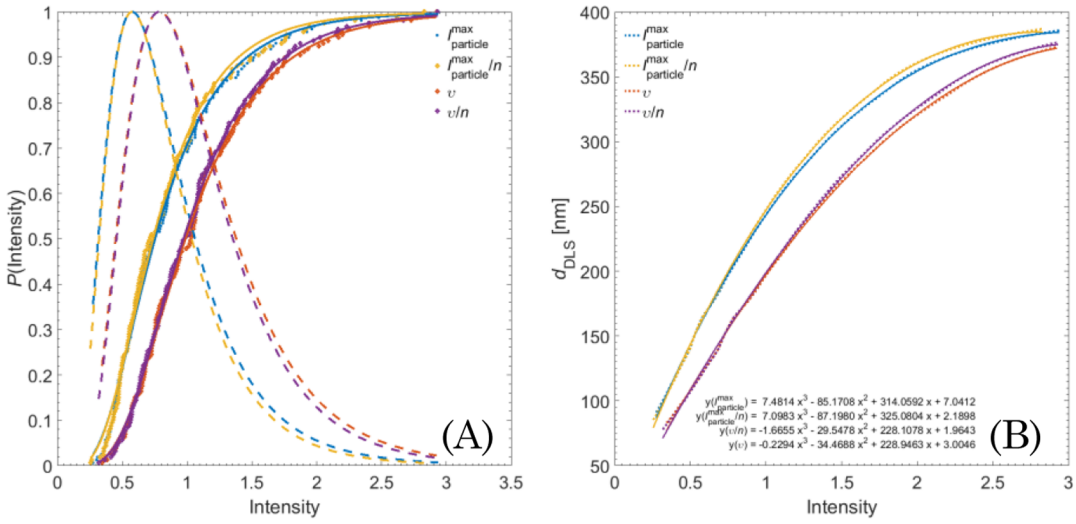

Figure 6. (A) ECDF (dots) with the best one-particle-type fit $P(x)$ (solid lines) and the corresponding probability distribution function (PDF, dashed lines) for parameters $I^{max}_{particle}$ (blue), $I^{max}_{particle}/n_c$ (yellow), υ (red), and υ/n_c (purple) for the liposome sample without GNPs on MUAM. (B) The relations between the PDFs of the fitted parameters (in panel A) with the d_{DLS} obtained with dynamic light scattering (DLS).

(PDF, dashed lines) for the parameters $I^{max}_{particle}$ (blue), $I^{max}_{particle}/n_c$ (yellow), υ (red), and υ/n_c (purple) for the liposome sample without GNPs on MUAM. Figure 6B shows the comparison between the PDFs of these parameters and the d_{DLS} obtained with DLS. This gives $d_{DLS} = O(x^3)$ with all test parameters, and all liposome samples. Furthermore, this result is well in accordance with the results by Halpern et al.,[10] since the relation $d \propto O(x^3)$ gives $O(x^3) \approx cx^3 \Leftrightarrow \log d \propto 3\log x$ with large intensities (compared with the intensities of the liposomes) such as presented in Halpern's paper.

CONCLUSION

SPRI microscopy has been used to study the properties of adsorbing liposomes of ≤200 nm in diameter with and without encapsulated GNPs. These liposomes are readily detectable in the SPRI microscope difference images on MUAM and streptavidin coated gold surfaces under water phase and at room temperature. The empirical cumulative distribution function (ECDF) is shown to follow a log-normal CDF that is typical for the liposome size distribution prepared with the extrusion method. When compared with the actual size distribution determined with DLS, we have shown that $d \propto O(x^3)$, that gives $\log d \propto 3 \log x$ with large intensities in accordance with the earlier results.[10] Also, the intensity maximum at the binding site can be used to detect differences in a set of particles. Such distinctions can be obtained from liposomes with encapsulated GNPs, which had clear deviation from the continuous one-particle-type fit. For the GNP-free liposomes, the one-particle-type was enough to explain the shape of the ECDF curve. The identification of the particles can be further improved by fitting the SPRI microscope patterns with the phenomenological equation given in this work (eq 22). This method gives a new intensity variable that was shown to consolidate the results of the measured intensities. At the same time, the wavenumber of the composite is obtained that also showed a diverging behavior with the GNP-liposomes on MUAM. Since this parameter relates to the propagating medium mostly outside the adsorbing particle, only the high intensity liposomes had a visible asymmetrical shift that also consolidated the intensity results. As a conclusion, the SPRI microscopy can be used to detect the encapsulated material inside the liposomes or another soft material, in addition to the extrinsic properties, such as the size distribution.

For the final remarks, we turn our attention to the future prospects of the SPRI microscopy method. At the moment, this technique can be assimilated with other label-free interfacial microscopy methods, such as scattering and interference microscopy.[25,26] These methods are highly sensitive, and they can be used to obtain crucial information even with the higher surface coverages that is not obtainable with the SPRI microscope at the moment. However, since SPRI microscope detects both singular particulates and their dielectric properties through analyses, and the surface engineering offers remarkable possibilities to study different binding and uptake mechanisms, the SPRI microscopy offers a very powerful analytical tool for the future interfacial analyses of soft nanomaterials surpassing many techniques with its versatility. It is also easy to predict that, like in the other SPR techniques, so-called multiparametric approaches; multiple wavelength excitations (see, e.g., 27); and measurements from different incident angles will eventually lead into more accurate and more revealing information about the material under study, also in the nanometer length scales.

ASSOCIATED CONTENT

Supporting Information

The Supporting Information is available free of charge on the ACS Publications website at DOI: 10.1021/acs.jpcc.6b09503.

I. Matlab Function: FFT image processing and the detection of nanostructures on the SPP Surface. II. Matlab script: the fitting of the single-particle SPRI microscope diffraction patterns. III. The determination of the liposome concentration after the gel filtration. IV. Size distribution and SPRI of liposomes. (PDF)

AUTHOR INFORMATION

Corresponding Author

*E-mail: lasse.murtomaki@aalto.fi. Tel: +358 50 5706352.

Notes

The authors declare no competing financial interest.

DOI: 10.1021/acs.jpcc.6b09503
J. Phys. Chem. C 2016, 120, 25958−25966

■ ACKNOWLEDGMENTS

The Academy of Finland is acknowledged for funding via the Programmable Materials Program "Light Triggered Nanoparticles" (OMA, #263453). National Science Foundation is acknowledged for the financial support through the Grant CHE-1403506 (RMC). L.V. thanks Mr. Yuhei Terada, Mr. Gerald Manuel, Ms. Kellen Kartub, and Mr. Brandon Matthews for their valuable help and fruitful discussions on the surface preparation techniques and with the SPRI measurements. This paper made use of the UCI laser facility premises run by Dmitry Fishman who is acknowledged for his help with the instruments.

■ REFERENCES

(1) Lee, H. J.; Wark, A. W.; Corn, R. M. Creating Advanced Multifunctional Biosensors with Surface Enzymatic Transformations. *Langmuir* **2006**, *22*, 5241−5250.
(2) Kano, H.; Mizuguchi, S.; Kawata, S. Excitation of Surface-Plasmon Polaritons by a Focused Laser Beam. *J. Opt. Soc. Am. B* **1998**, *15*, 1381−1386.
(3) Kano, H.; Knoll, W. A Scanning Microscope Employing Localized Surface-Plasmon-Polaritons as a Sensing Probe. *Opt. Commun.* **2000**, *182*, 11−15.
(4) Weichert, F.; Gaspar, M.; Timm, C.; Zybin, A.; Gurevich, E.; Engel, M.; Müller, H.; Marwedel, P. Signal Analysis and Classification for Surface Plasmon Assisted Microscopy of Nanoobjects. *Sens. Actuators, B* **2010**, *151*, 281−290.
(5) Zybin, A.; Kuritsyn, Y. A.; Gurevich, E. L.; Temchura, V. V.; Überla, K.; Niemax, K. Real-Time Detection of Single Immobilized Nanoparticles by Surface Plasmon Resonance Imaging. *Plasmonics* **2010**, *5*, 31−35.
(6) Gurevich, E.; Temchura, V.; Überla, K.; Zybin, A. Analytical Features of Particle Counting Sensor Based on Plasmon Assisted Microscopy of Nano Objects. *Sens. Actuators, B* **2011**, *160*, 1210−1215.
(7) Huang, B.; Yu, F.; Zare, R. N. Surface Plasmon Resonance Imaging using a High Numerical Aperture Microscope Objective. *Anal. Chem.* **2007**, *79*, 2979−2983.
(8) Shan, X.; Wang, S.; Tao, N. Study of Single Particle Charge and Brownian Motions with Surface Plasmon Resonance. *Appl. Phys. Lett.* **2010**, *97*, 223703.
(9) Wang, S.; Shan, X.; Patel, U.; Huang, X.; Lu, J.; Li, J.; Tao, N. Label-Free Imaging, Detection, and Mass Measurement of Single Viruses by Surface Plasmon Resonance. *Proc. Natl. Acad. Sci. U. S. A.* **2010**, *107*, 16028−16032.
(10) Halpern, A. R.; Wood, J. B.; Wang, Y.; Corn, R. M. Single-Nanoparticle Near-Infrared Surface Plasmon Resonance Microscopy for Real-Time Measurements of DNA Hybridization Adsorption. *ACS Nano* **2014**, *8*, 1022−1030.
(11) Cho, K.; Fasoli, J. B.; Yoshimatsu, K.; Shea, K. J.; Corn, R. M. Measuring Melittin Uptake into Hydrogel Nanoparticles with Near-Infrared Single Nanoparticle Surface Plasmon Resonance Microscopy. *Anal. Chem.* **2015**, *87*, 4973−4979.
(12) Maley, A. M.; Terada, Y.; Onogi, S.; Shea, K. J.; Miura, Y.; Corn, R. M. Measuring Protein Binding to Individual Hydrogel Nanoparticles with Single Nanoparticle SPRI Microscopy. *J. Phys. Chem. C* **2016**, *120*, 16843−16849.
(13) Lajunen, T.; Viitala, L.; Kontturi, L.; Laaksonen, T.; Liang, H.; Vuorimaa-Laukkanen, E.; Viitala, T.; Le Guével, X.; Yliperttula, M.; Murtomäki, L. Light Induced Cytosolic Drug Delivery from Liposomes with Gold Nanoparticles. *J. Controlled Release* **2015**, *203*, 85−98.
(14) Mura, S.; Nicolas, J.; Couvreur, P. Stimuli-Responsive Nanocarriers for Drug Delivery. *Nat. Mater.* **2013**, *12*, 991−1003.
(15) Viitala, L.; Pajari, S.; Lajunen, T.; Kontturi, L.; Laaksonen, T.; Kuosmanen, P.; Viitala, T.; Urtti, A. O.; Murtomäki, L. Photothermally Triggered Lipid Bilayer Phase Transition and Drug Release from Gold Nanorod and Indocyanine Green Encapsulated Liposomes. *Langmuir* **2016**, *32*, 4554−4563.
(16) Novotny, L.; Hecht, B.; Pohl, D. Interference of Locally Excited Surface Plasmons. *J. Appl. Phys.* **1997**, *81*, 1798−1806.
(17) Greffet, J.; Carminati, R. Image Formation in Near-Field Optics. *Prog. Surf. Sci.* **1997**, *56*, 133−237.
(18) Søndergaard, T.; Bozhevolnyi, S. I. Vectorial Model for Multiple Scattering by Surface Nanoparticles Via Surface Polariton-to-Polariton Interactions. *Phys. Rev. B: Condens. Matter Mater. Phys.* **2003**, *67*, 165405.
(19) Evlyukhin, A.; Bozhevolnyi, S. Point-Dipole Approximation for Surface Plasmon Polariton Scattering: Implications and Limitations. *Phys. Rev. B: Condens. Matter Mater. Phys.* **2005**, *71*, 134304.
(20) Gradshteyn, I. S.; Ryzhik, I. M. *Table of Integrals, Series, and Products*; Elsevier Inc.: London, 2015.
(21) Hansen, W. N. Electric Fields Produced by the Propagation of Plane Coherent Electromagnetic Radiation in a Stratified Medium. *J. Opt. Soc. Am.* **1968**, *58*, 380−388.
(22) Watanabe, K.; Horiguchi, N.; Kano, H. Optimized Measurement Probe of the Localized Surface Plasmon Microscope by using Radially Polarized Illumination. *Appl. Opt.* **2007**, *46*, 4985−4990.
(23) Schmidt, M.; Lipson, H. Distilling Free-Form Natural Laws from Experimental Data. *Science* **2009**, *324*, 81−85.
(24) Gheorghiu, S.; Coppens, M. O. Heterogeneity Explains Features of "Anomalous" Thermodynamics and Statistics. *Proc. Natl. Acad. Sci. U. S. A.* **2004**, *101*, 15852−15856.
(25) Andrecka, J.; Spillane, K. M.; Ortega-Arroyo, J.; Kukura, P. Direct Observation and Control of Supported Lipid Bilayer Formation with Interferometric Scattering Microscopy. *ACS Nano* **2013**, *7*, 10662−10670.
(26) Agnarsson, B.; Lundgren, A.; Gunnarsson, A.; Rabe, M.; Kunze, A.; Mapar, M.; Simonsson, L.; Bally, M.; Zhdanov, V. P.; Höök, F. Evanescent Light-Scattering Microscopy for Label-Free Interfacial Imaging: From Single Sub-100 Nm Vesicles to Live Cells. *ACS Nano* **2015**, *9*, 11849−11862.
(27) Granqvist, N.; Liang, H.; Laurila, T.; Sadowski, J.; Yliperttula, M.; Viitala, T. Characterizing Ultrathin and Thick Organic Layers by Surface Plasmon Resonance Three-Wavelength and Waveguide Mode Analysis. *Langmuir* **2013**, *29*, 8561−8571.

DOI: 10.1021/acs.jpcc.6b09503
J. Phys. Chem. C 2016, 120, 25958−25966